Spectroscopic study of milled MnF$_2$ nanoparticles. Size-and-strain-induced

photoluminescence enhancement

Spectroscopic study of milled MnF_2 nanoparticles. Size-and-strain-induced photoluminescence enhancement

Ignacio Hernández and Fernando Rodríguez[1]

DCITIMAC, Facultad de Ciencias, Universidad de Cantabria, 39005 Santander, Spain

E-mail: rodriguf@unican.es

Abstract

This work presents a correlated structural and spectroscopic study on ball-milled MnF_2. The aims are to produce impurity-lean particles through particle-size reduction leading to room-temperature photoluminescence (PL) and to modify the electronic states of the emitting centres. Despite non-radiative centres being still present, the PL quenching temperature was increased nearly 80 K, from 120 to 200 K, following this method. Milled MnF_2 has particle sizes down to several nanometres, and structural changes from the initial α-TiO_2 structure to the α-PbO_2 phase. Milling favours the presence of adsorbed water on the nanoparticle surface. Time-resolved spectroscopy indicates that the nanoparticle PL consists of a significantly inhomogeneous broadened band with respect to the initial MnF_2 PL. The temperature dependence of the lifetime measured at different wavelengths of the emission spectrum indicates the presence of several PL centres, the population of which is controlled by exciton migration and trapping. The widespread occurrence of emitting centres is explained in terms of milling-induced strains, the coexistence of two different structural phases, and the presence of adsorbed water molecules.

(Some figures in this article are in colour only in the electronic version)

1. Introduction

Transition-metal ions are commonly used as efficient photoluminescence (PL) centres in compounds like $(Ca, Mg)F_2$: Mn^{2+} [1–3], Al_2MgO_4: Co^{2+} [4], $KMgF_3$: Ni^{2+} [5, 6], MgF_2: Co^{2+} [3, 7], Al_2O_3: Cr^{3+} [8, 9], Al_2O_3: Ti^{3+} [10, 11], or $YAlO_3$: Mn^{3+} [12, 13]. For this reason, transition-metal-doped materials have received considerable attention for their capability as scintillators, optical sensors, memories, laser media, etc [14, 15]. However, the use

---

[1] Author to whom any correspondence should be addressed.

of PL systems based on concentrated transition-metal compounds at room temperature (RT) is very limited despite their high PL efficiency at low temperature. As is well known, an increase of the transition-metal concentration usually leads to PL quenching below room temperature in most concentrated materials. Pure transition-metal fluorides and oxides such as MnF_2, CoF_2, NiF_2, Cr_2O_3, Ti_2O_3, Mn_2O_3 illustrate this behaviour [8, 15, 16]. The dissimilar non-radiative de-excitation in concentrated materials was explained, many years ago, in terms of thermally activated exciton migration and subsequent transfer to non-radiative traps (exciton capture centres), which are eventually responsible for the absence of room-temperature PL [8, 16]. The usual strategies aiming to develop new methods for the control of exciton migration and trapping are mainly focused on the passivation of non-radiative traps through purification or doping with efficient PL centres [17, 18]. MnF_2 has been a model material for investigating exciton migration and trapping through selective doping with alkaline-earth and rare-earth traps acting as centres for exciton capture and selective emission [16–22].

MnF_2 shows an intense PL band peaking at 2.19 eV (566 nm) at 10 K that progressively quenches and redshifts upon heating to 120 K. A similar decrease of the PL lifetime occurs, passing from $\tau = 34$ ms at 10 K to $\tau = 0.2$ ms at 140 K. This behaviour has been explained on the basis of exciton migration and trapping by progressively deeper Mn^{2+}-trap centres with increasing temperature [8, 16]. Shallow Mn^{2+} traps are unable to retain the excitation, and migrate along the crystal until it is trapped in deeper Mn^{2+}-trap centres. The total de-excitation probability for the ith PL Mn^{2+}-trap centre can be written:

$$w_i(T) = \tau_i^{-1}(T) = w_{rad}^{(i)} + p^{(i)} \cdot \exp(-E_a^{(i)}/k_B T) \tag{1}$$

where the activation energy for exciton detrapping, $E_a^{(i)}$, is related to the energy depth of the perturbed $^4T_1$ PL state with respect to the unperturbed $^4T_1$ exciton. $w_{rad}^{(i)}$ accounts for the radiative transition probability and $p^{(i)}$ is the frequency factor for energy transfer, which is related to the Mn–Mn exchange interaction responsible for energy transfer. With increasing temperature, excitons are progressively trapped in deeper PL traps (i.e. higher E_a) and, eventually, transferred to non-radiative centres, which are responsible for the PL quenching [8].

Several Mn^{2+} traps have been identified to govern the PL behaviour of pure MnF_2 in the 10–120 K temperature range. In the low-temperature regime, these traps correspond to regular Mn^{2+} ions perturbed by next-nearest Zn^{2+}, Mg^{2+} and Ca^{2+} impurities. Their associated activation energies are, 8, 10 and 38 meV, respectively [22]. In the 40–120 K range, the PL band shifts to 2.05 eV (605 nm) and is associated with Mn^{2+} centres coordinated to at least one O^{2-} or OH^-, its activation energy being 130 meV [23]. The temperature dependence of this band indicates that PL is quenched for $T > 120$ K in the purest MnF_2 single crystal [19, 23]. Unavoidable traces of Mn^{3+} in the as-grown crystals have been proposed as likely non-PL traps. The interpretation is based on the non-radiative nature of Mn^{3+} in fluorides at room temperature, and the efficient transfer rate expected for Mn^{2+}–Mn^{3+} since the first $(MnF_6)^{3-}$ absorption band completely overlaps the relaxed Mn^{2+} $^4T_1$ excited state [24]. Although no trace of Mn^{3+} was detected in MnF_2 by optical absorption, its presence cannot be ruled out as an effective charge compensator for unavoidable O^{2-} and OH^- impurities [23].

Interestingly, high-pressure techniques have recently been employed to induce two-colour PL in pure MnF_2 at RT [25, 26]. This remarkable phenomenon appeared as a consequence of the pressure-induced structural changes in MnF_2, leading to local structure modifications around Mn^{2+} and in Mn–Mn pathways that reduce the exciton transfer and increase of the PL transition probability [25, 26].

In this work we present a different approach to achieve the goal of increasing PL efficiency in MnF_2. In particular, we look for new PL phenomena in MnF_2 induced by particle-size reduction through milling. This method enables us to induce slight modifications of the Mn^{2+}

Table 1. Structural parameters for the investigated MnF_2 samples as a function of the milling time. The relative abundance of the α-TiO_2-type and α-PbO_2-type phases in milled MnF_2 (see text) has been obtained by fitting the x-ray powder diffractogram $I(2\theta)$ using the FullProf program [27]. The particle size has been derived from the Bragg peak broadening through the Scherrer formula, taking into account the strain-broadening effects. Lattice parameters and average Mn–F distances of the Mn^{2+} octahedron for each phase have been obtained by Rietveld refinement. Note that the lattice volumes, $V = 79$ Å^3 for α-TiO_2 phase ($Z = 2$) and $V = 156$ Å^3 for the α-PbO_2 phase ($Z = 4$), do not vary appreciably with the milling time.

(a)

Milling time (h)	% α-TiO_2 phase	Grain size (nm)	Lattice parameters (Å) for $P4_2/mnm$ phase	$\langle d_{Mn^{2+}-F^-}\rangle$ (Å)
0	100	>1000	$a = 4.871 \pm 0.005$ $c = 3.310 \pm 0.005$	2.16
50	65	100	$a = 4.88 \pm 0.02$ $c = 3.31 \pm 0.02$	2.13
100	55	11	$a = 4.88 \pm 0.03$ $c = 3.31 \pm 0.03$	2.13
175	45	3	$a = 4.89 \pm 0.05$ $c = 3.32 \pm 0.04$	2.12

(b)

Milling time (h)	% α-PbO_2 phase	Grain size (nm)	Lattice parameters (Å) for $Pbcn$ phase	$\langle d_{Mn^{2+}-F^-}\rangle$ (Å)
0	0	—	—	
50	35	70	$a = 4.95 \pm 0.05$ $b = 5.81 \pm 0.05$ $c = 5.42 \pm 0.05$	2.28
100	45	3	$a = 4.89 \pm 0.05$ $b = 5.89 \pm 0.05$ $c = 5.43 \pm 0.05$	2.22
175	55	2	$a = 4.85 \pm 0.06$ $b = 5.90 \pm 0.06$ $c = 5.46 \pm 0.06$	2.20

electronic structure through phase transformation, and also provides a significant concentration of impurity-lean particles, depending on the impurity content of the starting MnF_2 material and the final particle size. If the nominal impurity concentration in the as-grown material is C(%), then the rate of impurity-lean particles, N_{LP}, with respect to the total number of particles, N, with an average size, L, is given by $\frac{N_{LP}}{N} \approx (1 - C \times 10^{-2})^{2\frac{L^3}{a^2c}}$. The exponent is the number of Mn^{2+} in the nanoparticle. The lattice parameters a and c are given in table 1(a) accounts for the MnF_2 molecules in the rutile unit cell. This relation establishes that 0.1% of the nanoparticles are free of impurities if $L = 3$ nm and $C = 1$%. This ratio increases to 50% if $L = 1.5$ nm.

Besides the grain size reduction, milling produces a significant strain effect in the nanoparticle that can locally modify the Mn^{2+} crystal field, giving rise to inhomogeneous band broadening and thus a wide distribution of activation energies for the Mn^{2+} emitting centres.

3
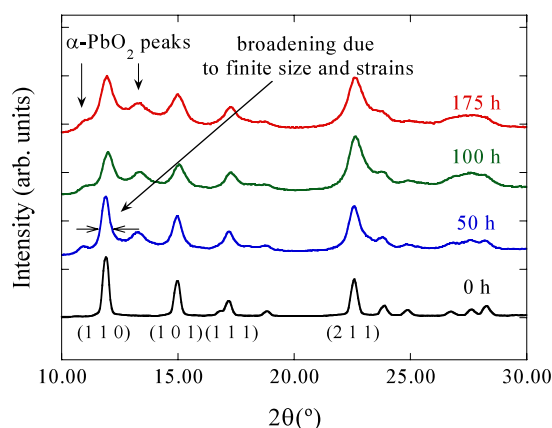
Figure 1. X-ray diffractograms, $I(2\theta)$, for as-grown (black) and milled MnF_2. Bragg peaks in the as-grown sample correspond to the α-TiO_2 phase (significant (h, k, l) values are included). New Bragg peaks appear in milled MnF_2 for milling times of 50, 100 and 175 h, due to the shear-induced phase transition to α-PbO_2 phase [30]. The Bragg peaks in milled MnF_2 are broadened with respect to the as-grown sample, indicating particle-size reduction and strains. A Mo tube ($\lambda_{K\alpha 1} = 0.709\,30$ Å and $\lambda_{K\alpha 2} = 0.713\,59$ Å) was used in the x-ray diffraction experiments.

2. Experimental details

MnF_2 crystals (Alfa Aesar, 99% purity) were used as starting material to transform into nanoparticles. The MnF_2 nanoparticles were obtained by milling using a Retsch PM 400/2 planetary ball-mill with tungsten carbide spheres using a ball-to-sample mass ratio, $m_{spheres}/m_{sample} = 10$. The milling was done at 200 rpm in cycles of 90 min, stopping for 60 min for cooling. The crystal structure was checked by x-ray diffraction with a Bruker D8 Advance diffractometer operating in a θ–θ Bragg–Bentano mode, and the structural characterization, including lattice parameters, atomic positions and phase ratio, was performed by Rietveld refinement using the FullProf software package [27]. The particle size was determined from the Bragg peak broadening through the Scherrer relation [28] including strain effects. Optical absorption (OA) and Fourier-transform infra-red absorption (FTIR) were obtained using a Perkin-Elmer Lambda 9 and a Nicolet Nexus 870 spectrophotometer, respectively. PL spectra as well as lifetime measurements were done using an ISA Fluoromax-2 fluorometer and a Chromex 500IS monochromator with a Tektronix 2430A oscilloscope, respectively; the light was detected with a Hamamatsu R928 photomultiplier. A Vibrant B 355 II OPO laser was used as an excitation source for time-resolved emission and excitation spectra as well as for lifetime measurements in the 407–700 nm range. A Scientific Instruments 202 closed-circuit cryostat with an APD-K controller was used for temperature dependence studies in the 10–300 K range.

3. Results and discussion

3.1. Structural characterization

Figure 1 shows the x-ray diffractograms of as-grown MnF_2 and of samples milled for 50, 100 and 175 h. The x-ray diffraction diagram $I(2\theta)$ was refined in terms of the α-TiO_2-type structure (tetragonal, $P4_2/mnm$) obtaining the structural parameters shown in table 1. They agree with those given elsewhere [29]. The diffraction patterns of milled samples present

remarkable differences with respect to the original sample: (1) all peaks are broadened, and (2) new peaks, which are absent in as-grown MnF_2 (α-TiO_2), appear in all milled samples. Although these phenomena are common to all investigated milled samples, it is worth noting that both the intensity of the new peaks and the peak broadening increase with the milling time. The new peaks correspond to the shear-induced phase transformation in MnF_2 from α-TiO_2 type to α-PbO_2 type (orthorhombic, *Pbcn*), as was already observed for long-time milling [30]. The α-PbO_2 phase (scrutynite) can be seen as an intermediate phase between the original α-TiO_2 (rutile) and α-$PbCl_2$ (cotunnite), the latter phase being the structural high-pressure modification of MnF_2 ($P > 14$ GPa at RT) [31]. The occurrence of such a metastable α-PbO_2 phase has already been observed in high-pressure experiments upon downstroke or under shear stresses [26, 30, 31].

X-ray diffraction diagram refinement using the FullProf methodology [27, 32] provides a suitable structural characterization of the milled samples: the relative abundance of each phase α-TiO_2 and α-PbO_2, and the lattice parameters (table 1). We observe that the lattice parameters are very similar for all milled samples although, despite the experimental error, a slight increase of the volume seems to occur in both phases with the milling time. On the other hand, the average Mn–F distance derived from the atomic positions decreases with milling time. It must be noted that the average Mn–F distance in the α-PbO_2 phase is around 10 Å longer than in the α-TiO_2, for which the MnF_6 octahedron is more distorted.

The structural characterization from x-ray diffraction also provides information on the particle size through the Scherrer formula [28], taking into account that broadening is caused jointly by size and stress effects. The so-obtained particle sizes (table 1) diminish notably on passing from 100 to 3 nm with the milling time from 50 to 175 h for the α-TiO_2 phase. Analogously, the α-PbO_2 phase shows a similar behaviour, with a particle size ranging from 70 nm for 50 h milling to 2 nm for 175 h. It must be noted that the present method is not able to distinguish whether the particles are single-phased or whether both α-TiO_2 and α-PbO_2 phases coexist in a given MnF_2 particle. Taking into account the unexpectedly low so-obtained particle sizes we conclude that the latter hypothesis is likely. On the basis of a phase-coexistence particle, we can estimate the actual particle size as a function of the relative abundance of each phase parameter α. Thus the real average particle size roughly corresponds to $2[\alpha \cdot R_{\text{rutile}} + (1 - \alpha) R_{\text{scrutynite}}]$. Accordingly, the particle would consist of two coexisting phases within a size of about 200, 100 and 10 nm for milling times of 50, 100 and 175 h, respectively. A structural characterization study in order to confirm the present estimates using electron microscopy is currently in process.

3.2. Spectroscopic study of MnF$_2$ nanoparticles

OA and FTIR measurements provide additional information on the MnF_2 nanoparticles. The OA spectra of milled MnF_2 samples are very similar, and show the characteristic absorption bands due to the $^6A_1 \rightarrow \Gamma_i$ electronic transitions within MnF_6^{4-}. Γ_i stands for the final excited state involved in the transition: $\Gamma_i = {}^4T_1, {}^4T_2, {}^4A_1, {}^4E\ldots$. The OA spectrum for 100 h milled MnF_2 together with the single-crystal one for comparison purposes are shown in figure 2. The spectrum appears settled on an important dispersion background from the powder sample. Interestingly, the ^4A, ^4E narrow band for all milled samples shifts by 0.03 eV towards lower energies with respect to the single crystal ^4A, ^4E energy (3.14 eV). Such a significant redshift fact experienced by the crystal-field-independent ^4A, ^4E band likely indicates the presence of at least one OH^- or O^{2-} ligand in the Mn^{2+} coordination. Therefore, we can assume that an important fraction of MnF_5O^{5-} or MnF_5OH^{4-} complexes have been formed by hydration in the particles. Given that there is no trace of heteroligand complexes in the nanoparticle
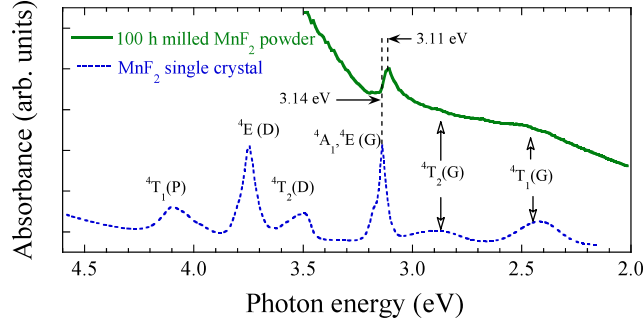
Figure 2. Optical absorption spectra of 100 h milled MnF_2 (black line) at room temperature and optical absorption as-grown MnF_2 single crystal (dotted), which is included for comparison purposes. The peaks are characteristic of the (quasi)-octahedral MnF_6^{4-} complex, and are labelled according to the O group symmetry notation. Note the energy shift of 0.03 eV towards lower energies for the $^6A_1(S) \rightarrow {}^4A_1, {}^4E(G)$ peak in milled MnF_2.

structure as derived from x-ray diffraction, we conclude that such complexes are probably formed on the particle surface. In fact, the redshift of 0.03 eV can be explained in terms of the higher covalency of the Mn–O bond, that reduces the Racah parameters B and C, and thus the $^6A_1 \rightarrow {}^4A_1, {}^4E$ transition energy, $E \approx 20B + 4C$ [33, 34]. FTIR spectroscopy confirms the presence of water molecules in the samples, by the presence of absorption bands at 1600 and 3330–3500 cm^{-1}. These bands correspond to the ν_2 mode and ν_1, ν_3 fundamentals of the water vibrations, respectively [35]. Despite water being present in the as-grown powder sample, hydration increases with the milling time in accordance to expectations based on the increase of the surface to bulk ratio attained upon decreasing the particle size.

The PL properties of as-grown MnF_2 are the same as those reported elsewhere [16, 22, 23]. The PL at $T = 10$ K is very intense and consists of a single broad band peaking at 2.19 eV (592 nm) with a radiative lifetime $\tau = 24$ ms (figure 3). The PL band progressively shifts towards lower energy with increasing temperature, their intensity $I(T)$ and PL lifetime $\tau(T)$ decreasing in the 10–120 K range. The PL energy and lifetime vary from 2.19 eV (592 nm) and 24 ms at $T = 10$ K to 2.05 eV (605 nm) and 10 ms at $T = 40$ K, and 1.98 eV (630 nm) and 0.2 ms at 100 K. PL quenches above 120 K. Moreover, the PL band between 20 and 90 K is strongly inhomogeneous, and consists of several components having different associated lifetimes. Accordingly, we have modelled the time-dependent behaviour of the MnF_2 emission at a given wavelength, λ, and temperature, T, through the equation

$$I(T, \lambda, t) = \sum_i I_i(T, \lambda, t) \qquad (2)$$

where $I_i(T, \lambda, t)$ corresponds to the ith intensity decay component that we associate with PL emitted from the ith Mn^{2+} trap. The spectral distribution $I_i(T, \lambda, t)$ peaks at λ_i, according to the trap depth, ΔE_i, with respect to the pure-exciton emission energy, E_{exc}. The ith emission band energy is thus given by $E_i = hc/\lambda_i = E_{exc} - \Delta E_i$, where h is the Planck constant, c the speed of light and λ_i the corresponding wavelength at the band maximum. The associated PL lifetime in terms of the transition probability $^4T_1 \rightarrow {}^4A$, $w_i(T)$ is given by equation (1), where the activation energy $E_a^{(i)}$ is related to ΔE_i. Therefore, we obtain

$$I_i(T, t) = I_0^{(i)}(\lambda) \cdot \exp\left(-\frac{t}{\tau_i(T)}\right). \qquad (3)$$

The PL is then governed by the thermal population and depopulation of progressively deeper Mn^{2+} traps whose emission is redshifted with respect to shallower trap emission, depending on
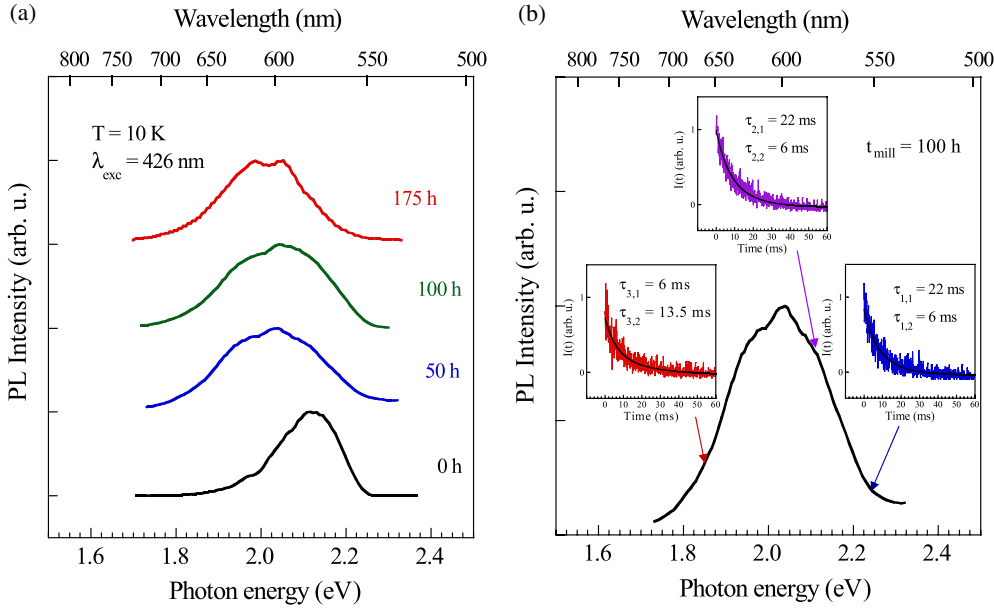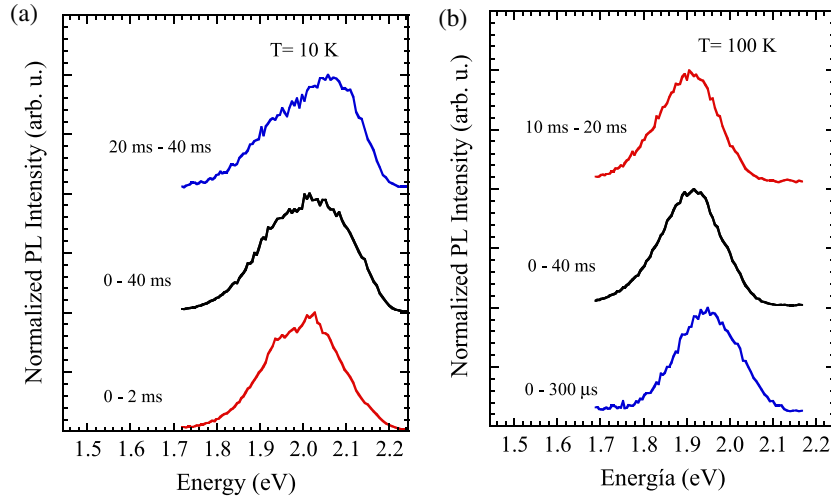
Figure 3. (a) Photoluminescence (PL) spectra at $T = 10$ K for 150, 100 and 175 h milled MnF_2 as well as for as-grown MnF_2. The excitation wavelength, $\lambda_{exc} = 426$ nm, populates the first $^4T_1$ excited state (see figure 2). (b) PL spectra of 100 h milled MnF_2 at $T = 18$ K using an excitation wavelength $\lambda_{exc} = 426$ nm. The insets show the PL intensity decay as a function of time, $I(E_{em}, t)$, at different emission energies: $E_{em,1} = 2.25$ eV (550 nm), $E_{em,2} = 2.10$ eV (590 nm) and $E_{em,3} = 1.85$ eV (670 nm). The associated lifetimes, $\tau_{i,1}$ and $\tau_{i,2}$, have been obtained by fitting to two exponential decays through the equation $I(E_{em,i}, t) = I_{i,1}(E_{em,i})e^{-t/\tau_{i,1}} + I_{i,2}(E_{em,i})e^{-t/\tau_{i,2}}$. The index 1 represents the most intense component and 2 refers to the weakest component for each emission energy, $E_{em,i}$.

the activation energy, $E_a^{(i)}$. Indeed, the activation energies for different Mn^{2+} traps in the as-grown MnF_2 have been obtained from $\tau_i(T)$, the values of which are $E_a = 5$, 50 and 250 meV, in fair agreement with previous findings [22, 23].

Milled MnF_2 shows a different PL behaviour compared to as-grown MnF_2. The PL spectrum at $T = 10$ K consists of a inhomogeneously broadened band at 2.05 eV (600 nm) with a full width at half maximum (FWHM) of 0.3 eV (80 nm), as is shown in figure 3(a). We observe similar emission bands for all milled samples, but the band shape appears enhanced to lower energies for longer milling times. Lifetime measurements performed at different wavelengths of the band confirm the inhomogeneous band broadening, which is even important at low temperature, in contrast to as-grown MnF_2. Figure 3(b) shows the PL band at $T = 20$ K for 100 h milled MnF_2 and the corresponding decays for different wavelengths over the band. The time dependence of the PL intensity, $I(\lambda, t)$, is different at $\lambda = 1.85$, 2.10 and 2.25 eV (670, 590 and 550 nm, respectively). Nevertheless, the emission band components, $I_i(\lambda, T, t)$, overlap at the selected wavelengths. Thus, we conclude that the PL band actually consists of several single overlapping bands, each corresponding to the emission from the ith perturbed Mn^{2+} centre, which has been excited either from the excitation beam or by energy transfer from excited nearby Mn^{2+}. The observed variations for all milled MnF_2 can be explained within this model through changes of the intensity and associated PL lifetime for each ith emission component.

Figure 4. Time-resolved photoluminescence spectra for 100 h milled MnF$_2$ at $T = 10$ K (a) and 100 K (b). Time delays after laser pulse, Δt, and counting time, t_{count}, are shown on the left side of each spectrum, respectively.

The variation of the PL band with temperature for milled samples is analogous to that of as-grown MnF$_2$: the lower-energy sideband becomes more intense in comparison to the higher-energy sideband (i.e. the band redshifts overall), whereas the PL lifetime decreases with increasing wavelength.

Time-resolved emission spectroscopy at $T \sim 10$ K (figure 4(a)) indicates that milled MnF$_2$ PL shifts to higher energies when the counting delay time is increased (long-lived components). The band peaks at 2.1 eV for a delay of 20 ms in contrast to the observed behaviour in the intermediate temperature regime, $T \sim 100$ K, in which the spectrum associated to the long-lived components is located at 1.9 eV, and thus redshifts at higher temperatures (figure 4(b)).

Despite the problem difficulty, we can qualitatively explain the temperature variation of PL for milled MnF$_2$ on the basis of an exciton-migration scheme. Milling produces a lot of strain-perturbed Mn^{2+}-emitting traps in MnF$_2$ that can retain excitons at a given temperature, according to their activation energy (equation (1)). It yields a broad distribution of Mn^{2+} traps due to size reduction, the stress field and the induced structural phase transitions. All these traps govern the PL behaviour and its temperature dependence. Therefore, the PL spectrum shows an important inhomogeneous broadening, whose centroid progressively redshifts with increasing temperature. The PL band energy and the corresponding lifetime for the 100 h milled MnF$_2$ decrease with temperature from $E = 2.1$ eV ($\lambda = 590$ nm) and $\tau = 24$ ms at 10 K to $E = 1.92$ eV ($\lambda = 640$ nm) and $\tau = 100$ μs at 100 K.

The present model also explains why in the intermediate-temperature regime ($T \sim 100$ K), shorter lifetimes correspond to higher energies while longer lifetimes are observed in the lower-energy sideband, i.e. higher activation energies (equation (3)). The transition probability, w_i, in equation (1) becomes larger as the temperature increases for most shallow traps, since E_a is small. However, deeper traps, i', obeying $w_{rad}^{(i')} > w_{rad}^{(i)}$, would emit with shorter lifetimes at low temperature; however, they can emit with longer lifetimes than the shallow traps since $\tau_{i'}^{-1}(T) < \tau_i^{-1}(T)$ at higher temperatures. This reflects that the transfer probability for trap depopulation is more important for shallow traps in comparison to deeper traps that eventually are able to retain the excitation, thus favouring longer emission lifetimes. When the temperature
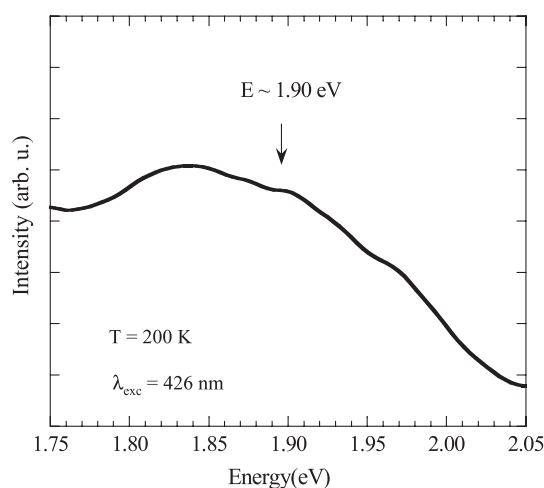
Figure 5. Photoluminescence spectrum at $T = 200$ K corresponding to the 175 h milled MnF_2 upon laser excitation at $\lambda_{exc} = 426$ nm. The emission band is very inhomogeneous and corresponds to deep photoluminescent Mn^{2+} traps (see text).

increases high enough, the PL traps are not able to retain excitons that migrate away until they are captured by non-radiative centres or impurities, yielding PL quenching. We have observed such PL behaviour in all milled samples. Mn^{2+} at the nanoparticle surface involving water molecules as ligands can act as non-PL centres, since water molecules are known to be efficient centres for non-radiative relaxation, and thus they can partially account for PL quenching of the particle. Water molecules are responsible for the absence of PL in Mn^{2+} aqueous solutions and other hydrated materials [33, 35].

Despite the presence of non-radiative de-excitation centres in the nanoparticle, the increase of the quenching temperature is noteworthy. In fact, we have detected a strongly redshifted emission at $T = 220$ K in the 175 h milled MnF_2. This means that the quenching temperature increases by at least $\Delta T = 100$ K upon milling (figure 5). This salient result foresees the possibility of achieving RT emission through the proposed milling methodology, which is able to provide both a significant fraction of impurity-lean particles and deep PL Mn^{2+} traps, both enhancing PL at high temperatures.

Aiming to reveal the nature of the deep PL traps, we have performed time-resolved excitation spectroscopy associated with bands at 2.14 eV (580 nm) and 1.88 eV (660 nm) at 10 K, using delays of 20 and 0 ms after the laser pulse and counting times of 20 and 5 ms, respectively. The results are shown in figure 6 for the 100 h milled MnF_2. Although both excitations are similar, we observe a slight blueshift of 20 meV in the first $^6A_1 \rightarrow {}^4T_1$ excitation band for the 1.88 eV emission. Given that the band energy depends on the crystal field as -10 Dq, we conclude that the excitation spectra correspond to similar but structurally different Mn^{2+} sites. Since 10 Dq depends on the Mn–F distance, R_{Mn-F}, as 10 Dq $\sim R_{Mn-F}^{-n}$, with $n \sim 5$ for Mn^{2+} in fluorides [36], we deduce that the variation of 10 Dq obtained from the excitation spectra probably reflects slightly different R_{Mn-F} values. Taking the energy shift of 20 meV, we conclude that R_{Mn-F} for the Mn^{2+} centre emitting at 2.14 eV is about 1 pm shorter than R_{Mn-F} for the Mn^{2+} centre emitting at 1.88 eV. However, it must be noted that, although time-resolved excitation spectroscopy is a selective method for studying different sites, the present estimates must be considered as an underestimation of the actual R_{Mn-F} since the emission
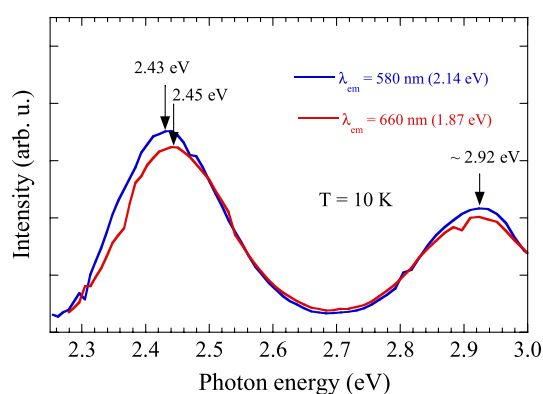
Figure 6. Time-resolved excitation spectra for 100 h milled MnF_2 at $T = 10$ K. They were obtained at emission energies of 2.14 eV (580 nm) and 1.87 eV (660 nm). The excitation spectrum associated with the 2.14 eV emission was taken using $t_{count} = 20$ ms and $\Delta t = 20$ ms. The excitation spectrum of the 1.87 eV emission was obtained with $t_{count} = 5$ ms and $\Delta t = 0$.

bands overlap and the corresponding excitation bands have unavoidable contributions from the two Mn^{2+} centres.

4. Conclusions

We have structurally characterized milled MnF_2 samples. Milling decreases the particle size and induces a phase transformation from α-TiO_2 MnF_2 to α-PbO_2 MnF_2 up to 55% for 175 h milling time. Both phases are likely to coexist in the nanoparticle, but the Mn^{2+} coordination geometry and Mn–F distance slightly change in each phase. The main difference between the PL spectra of the milled and as-grown MnF_2 at 10 K is the inhomogeneous band broadening, and the enhancement of the low-energy sideband in the milled samples. The temperature dependence of the MnF_2 nanoparticle PL can be described in terms of exciton migration and trapping in a broad distribution of deep Mn^{2+} traps. The PL-quenching temperature increases nearly 100 K for milled MnF_2 with respect to as-grown MnF_2. RT emission was not achieved due to the presence of non-radiative traps, among which adsorbed water molecules have been unambiguously identified.

Acknowledgments

References

[1] Rodríguez F *et al* 2003 *J. Chem. Phys.* **119** 8686
[2] Hernández I and Rodríguez F 2003 *Phys. Rev.* B **67** 012101
[3] Suzuki Y *et al* 1987 *Phys. Rev.* B **35** 4472
[4] Malyarevich A M *et al* 2002 *J. Opt. Soc. Am.* B **19** 1815
[5] Sturge M D 1971 *Solid State Commun.* **9** 899

 [6] Mortier M *et al* 2003 *Phys. Rev.* B **67** 115126
 [7] Zhang Z M *et al* 2002 *Appl. Opt.* **41** 1071
 [8] Henderson B and Imbusch G F 1989 *Optical Spectroscopy of Inorganic Solids* (New York: Oxford University Press)
 [9] Burns R G 1993 *Mineralogical Applications of Cristal Field Theory* (*Cambridge Topics in Mineral Physics and Chemistry* vol 5) 2nd edn (Cambridge: Cambridge University Press)
[10] Moulton P F 1982 *Opt. News* **8** 9
[11] García-Revilla S *et al* 2005 *J. Phys.: Condens. Matter* **14** 447
[12] Kück S *et al* 1998 *Phys. Rev.* B **57** 2203
[13] Zhydachevskii Y *et al* 2006 *J. Phys.: Condens. Matter* **18** 5389
[14] Blasse G and Grabmaier B C 1994 *Luminescent Materials* (Berlin: Springer)
[15] Di Bartolo B 1968 *Optical Interactions in Solids* (London: Wiley)
[16] Holloway W W *et al* 1963 *Phys. Rev. Lett.* **11** 82
[17] Weber M J 2002 *J. Lumin.* **100** 35
[18] Wunsch F R and Gebhardt W 1989 *J. Phys.: Condens. Matter* **1** 855
[19] Tsuboi T, Silfsten P and Laiho R 1991 *Phys. Rev.* B **43** 1135
[20] Flaherty J M and Di Bartolo B 1973 *Phys. Rev.* B **8** 5232
[21] Di Bartolo B, Danko J and Pacheco D 1987 *Phys. Rev.* B **35** 6386
[22] Greene R *et al* 1968 *Phys. Rev.* **171** 600
[23] Rodríguez F *et al* 1985 *J. Physique Coll.* **46** (C7) 155
[24] Aguado F, Rodríguez F and Núñez P 2003 *Phys. Rev.* B **67** 205101
[25] Hernández I 2006 *PhD Thesis* University of Cantabria
[26] Hernández I, Rodríguez F and Hochheimer H D 2007 *Phys. Rev. Lett.* **99** 027403
[27] Rodríguez-Carvajal J 1993 *Physica* B **192** 55
[28] Suryanarayana C and Norton M G 1998 *X-ray Diffraction, a Practical Approach* ed C Suryanarayana and M G Norton (New York: Plenum)
[29] Dufek P, Schwarz K and Blaha P 1993 *Phys. Rev.* B **48** 12672
[30] Dachille F and Roy R 1960 *Nature* **186** 70
[31] Tonkov E Y 1992 *High Pressure Phase Transformations: A Handbook* (Philadelphia, PA: Gordon and Breach) and references therein
[32] Fernández L 2004 private communication
[33] Lever A B P 1984 *Inorganic Electronic Spectroscopy, Studies in Physical and Theoretical Chemistry* 2nd edn (New York: Elsevier)
[34] Griffith J S 1980 *The Theory of Transition Metal Ions* (Cambridge: Cambridge University Press)
[35] Eisenberg D and Kauzmann W 1969 *The Structure and Properties of Water* (London: Oxford University Press)
[36] Rodriguez F and Moreno M 1986 *J. Chem. Phys.* **84** 692